A theoretical study on the strong-field ionization of the lithium atom

2013 J. Phys. B: At. Mol. Opt. Phys. 46 115601

(http://iopscience.iop.org/0953-4075/46/11/115601)

J. Phys. B: At. Mol. Opt. Phys. **46** (2013) 115601 (9pp) doi:10.1088/0953-4075/46/11/115601

A theoretical study on the strong-field ionization of the lithium atom

Shih-Da Jheng and T F Jiang

Institute of Physics, National Chiao-Tung University, Hsinchu 30010, Taiwan

E-mail: tfjiang@faculty.nctu.edu.tw

Received 31 January 2013, in final form 20 April 2013
Published 9 May 2013
Online at stacks.iop.org/JPhysB/46/115601

Abstract

We apply a recently developed momentum space method (Jiang *et al* 2012 *Phys. Rev.* E **86** 066702) to investigate the experimental results of strong-field ionization of the lithium atom (Schuricke *et al* 2011 *Phys. Rev.* A **83** 023413). By splitting the photoelectron into groups of even and odd angular momenta and by using the states' population history, we can analyse the ionization mechanism in further detail. The lower energy double-peak structure, shown experimentally, of the photoelectron is attributed to the three-level Λ-coupling effect. The spectral difference of 10 and 30 fs pulses at a typical intensity is demonstrated. We explain why the strong-field ionization fluctuates at intensities of 6 and 10 fs, but not for a 30 fs pulse. The change of fan-like photoelectron angular distribution with intensity in direction parallel to polarization is explained. Use of the Keldysh parameter to classify the tunnelling and multiphoton ionization is not meaningful for the lithium atom, because the ground state is mostly depleted before reaching peak intensity.

(Some figures may appear in colour only in the online journal)

1. Introduction

A recent paper reported experimental results together with calculations on the strong-field ionization of the lithium atom [2]. The experimental work used new technology. Namely, (1) the experiment was performed in a magnetic-optical trap and the thermal effect was small; and (2) the reaction microscope technique was used to measure photoelectron spectra to reach a high resolution of ∼meV. In strong-field ionization, the Keldysh parameter $\gamma = \sqrt{\mathrm{IP}/2U_p}$ is used to classify the multiphoton ionization (MPI, $\gamma > 1$) and tunnelling ionization (TI, $\gamma < 1$), where IP is the ionization potential and $U_p = (\text{peak intensity})/4\omega^2$ with the laser central frequency ω. Because the lithium atom has a low ionization potential (5.39 eV), both MPI and TI are feasible at modest infrared (IR) laser intensity. In addition, the over-barrier ionization (OBI) occurs when the Coulomb barrier height is suppressed to reach the ground state energy by laser field. The classical estimation by dc field, the laser intensity for OBI is $\mathrm{IP}^4/16Z^2$. The OBI intensity for Li (3.4 TW cm^{-2}, $\gamma = 3.7$) is in the MPI regime not in the TI regime as in the inert gas atomic species. Thus, with the lithium target under experimental parameters, MPI, OBI and TI regimes are all covered.

In the experiment, a 30 fs full-width of half-maximum (FWHM) laser pulse with central wavelength of 785 nm and peak intensity in $10^{11} \sim 10^{14}$ W cm^{-2} were performed. The photoelectron angular distributions (PADs) and the above-threshold ionization (ATI) photoelectron spectra were shown [2]. At low intensity, the ATI is simply a non-resonant multiphoton ionization (NRMPI). At a stronger intensity, because of the larger ponderomotive shifts, the intermediate states might be populated and lead to a resonance-enhanced multiphoton ionization (REMPI) [3, 4]. A noticeable double-peak ATI appeared at low photoelectron energy. For peak intensities higher than 8×10^{12} W cm^{-2}, fan-like PADs appear. The long-range Coulomb interaction between the electron and its parent ion explains this structure [5, 6]. By calculating a wider range of intensities, we found that the fan-like structure changes in the direction parallel to polarization but not perpendicular. In addition, the change is closely related to ionization suppression with intensity. We perform calculations to examine the above mechanisms further.

For the aspect of calculation, the matrix iteration method (MIM) and the Arnoldi–Lanczos method (ALM) were presented in [2], where results of the time-dependent Schrödinger equation in coordinate space (R-TDSE) based on the model single-active electron (SAE) were given. To

compare the experimental results, focal volume averaging must be carried out. In MIM, a maximum radius of 3000 au was used to avoid the boundary reflection for higher intensity. In ALM, a box size of 2000 au with the transparent boundary condition was used. Angular momenta up to 20 $\sim$ 30 were included in both methods. However, the photoelectron spectra from the MIM and ALM were not in agreement. Our theoretical study would be helpful for understanding in this area.

This paper presents a momentum space TDSE (P-TDSE) calculation. Both R-space and P-space are simply alternative representations in quantum mechanics. In the R-space method, a finite spatial box is often used in numerical simulations. The method works effectively for the theoretical modeling of high-order harmonic generations (HHG), because the process mainly involves the scattering of a laser driven electron with its parent ion. A range of a few times of laser driven electron displacement is adequate for simulating the effects [7]. For another prominent ATI process, the finite-box method cannot provide complete information on the photoelectron wavepacket. Among the many advanced methods, Telnov and Chu developed the Kramers–Henneberger-like transform method [8, 9] for the ATI of the hydrogen atom under an intense long-wavelength laser field. Scrinzi *et al* developed the time-dependent surface flux method. A wide photoelectron energy range of ATI spectra were demonstrated and calibrated [10]. However the P-space representation has the essential advantage of no numerical boundary reflection in solving the TDSE. For scattering problems, the P-space does not require a huge box like the R-space method but has difficulties in application. A singularity is in the Coulomb kernel and the range of momenta is $p \in (0, \infty)$. The singularity was regularized by using the Lande subtraction method [11]. Recently, Zhou and Chu [12] performed an extensive study on the strong-field ionization of the hydrogen atom by using the Lande method. However, the range of momenta $p \in (0, \infty)$ inherent in analytic formulation is still inconvenient in calculations. Therefore, we modified the conventional Lande subtraction method and developed the finite integration limit P-TDSE. The improvement demonstrated that the method is efficient and accurate and is especially suitable for strong-field problems [1].

The paper is organized as follows: section 2 briefly describes the P-TDSE method. Section 3 presents the results and discussions. Finally, concluding remarks are given in section 4.

2. The time-dependent momentum space method

In the finite-integration limit momentum space method [1], the TDSE of a model one-electron atom under a laser field in R-space is transformed into P-space through Fourier transformations. The eigenset of the unperturbed Hamiltonian is then employed for time-propagation [13]. For the eigenstate problem, let

$$\Phi(\vec{p}) \equiv 1/(2\pi)^{\frac{3}{2}} \int \Psi(\vec{r})\, \mathrm{e}^{-\mathrm{i}\vec{p}\cdot\vec{r}} \mathrm{d}^3 r,$$
$$W(\vec{p}) \equiv 1/(8\pi^3) \int U(\vec{r})\, \mathrm{e}^{-\mathrm{i}\vec{p}\cdot\vec{r}} \mathrm{d}^3 r. \quad (1)$$

The eigenstate problem becomes

$$H_0\Phi(\vec{p}) \equiv \frac{p^2}{2}\Phi(\vec{p}) + \int W(\vec{p}-\vec{q})\Phi(\vec{q})\, \mathrm{d}^3 q = E\Phi(\vec{p}), \quad (2)$$

where H_0 is the Hamiltonian operator of the SAE atom and

$$W(\vec{p}) = \frac{-1}{2\pi^2 p^2} + W_{\mathrm{short}}(p), \quad (3)$$

where the first term in the right-hand side originates from the Coulomb potential and the $W_{\mathrm{short}}(p)$ is the Fourier transformation of the short-range potential part $V_{\mathrm{short}}(r)$. We reformulated the integration of momentum to work for $p \in (0, p_{\max})$ where $p_{\max} \sim 100$ au instead of $p \in (0, \infty)$ [1]. We have shown that using the proposed method improves the accuracy of low-lying hydrogen eigenenergies and eigenfunctions to several orders, as compared to the conventional Lande method [11]. In addition, the calculation is efficient and accurate. For the lithium atom, we used the following SAE mode potential [14]

$$\begin{aligned} U(r) &= -1/r + V_{\mathrm{short}}(r), \\ V_{\mathrm{short}}(r) &= -(2\mathrm{e}^{-a_1 r} + a_2 r \mathrm{e}^{-a_3 r})/r, \\ &\text{with } a_1 = 3.395,\ a_2 = 3.212 \text{ and } a_3 = 3.207. \end{aligned} \quad (4)$$

Because the energy level of the inner $1s^2$ core is far below the active 2s level (−5.39 eV), the lithium atom under IR light is nearly equivalent to a SAE atom. The low-lying bound levels were calibrated to NIST Atomic Spectra Database [15]. The updated accurate atomic transition properties of lithium were compiled by Wiese and Fuhr [16] including seven advanced calculations and several radiative lifetime measurements. For the lithium atom, the different theoretical results normally agree within 0.5% for the stronger transitions. The model potential we used is not quoted in [16]. However, Schweizer *et al* extensively listed their spectroscopic results and achieved excellent agreement with [16]. In table 1, we calculate some oscillator strengths that were not contained in [14] for supplement. Those results were generated by using the model potential [14], showing that the SAE model was appropriate for this study.

The P-TDSE under the dipole approximation can be derived as

$$\mathrm{i}\frac{\partial \Psi}{\partial t} = [H_0 + \vec{p}\cdot\vec{A}(t)]\Psi(\vec{p}, t). \quad (5)$$

The split-operator-algorithm [7, 13] is used for the time propagation:

$$\Psi(\vec{p}, t+\Delta) = \mathrm{e}^{-\mathrm{i}H_0\frac{\Delta}{2}} \mathrm{e}^{-\mathrm{i}\vec{p}\cdot\int_t^{t+\Delta}\vec{A}(t')\,\mathrm{d}t'} \mathrm{e}^{-\mathrm{i}H_0\frac{\Delta}{2}} \Psi(\vec{p}, t) + O(\Delta^3). \quad (6)$$

The prominent processes, such as the ATI and the HHG, can be simulated in P-TDSE. The P-space method provides a practical tool for strong-field problems in addition to the well-known R-space method and has the advantage of having no reflection of wavepacket from the numerical boundary. We

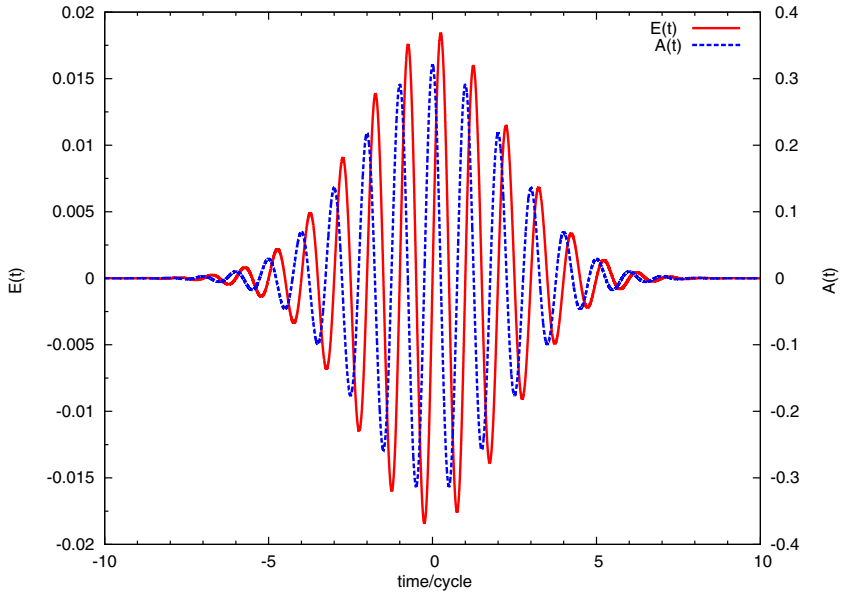

Figure 1. The profiles of the electric field $E(t)$ and the vector potential $A(t)$ of a 10 fs FWHM Gaussian pulse at peak intensity of 12 TW cm^{-2} and wavelength of 785 nm.

Table 1. Oscillator strengths of 2s $\rightarrow$ np and 2p $\rightarrow$ ns of the lithium atom calculated by using the SAE model potential of equation (4). Accurate data from [16] are also listed for comparison.

2s $\rightarrow$ np	By equation (4)	[16]	2p $\rightarrow$ ns	By equation (4)	[16]
2p	7.4653×10^{-1}	7.4696×10^{-1}	2s	-2.4884×10^{-1}	-2.48987×10^{-1}
3p	4.9777×10^{-3}	4.711×10^{-3}	3s	1.0985×10^{-1}	1.105×10^{-1}
4p	4.3948×10^{-3}	4.218×10^{-3}	4s	1.2719×10^{-2}	1.283×10^{-2}
5p	2.6184×10^{-3}	2.619×10^{-3}	5s	4.2703×10^{-3}	4.34×10^{-3}
6p	1.6272×10^{-3}	1.581×10^{-3}	6s	2.0154×10^{-3}	2.05×10^{-3}

applied the new P-space method to examine the laser excitation dynamics of the lithium atom. In our calculation we used 1024 grids in momentum and 15 angular momenta. The momentum $p \in (0, 100)$ was bilinearly mapped from Gauss–Lobatto–Legendre grids $x \in (-1, +1)$ as described in [1]. We used the strongest laser pulse of intensity 7×10^{13} W cm^{-2}, FWHM of 30 fs and wavelength of 785 nm in simulation as a convergence test. The final probability in the maximum angular momentum states is 4.1×10^{-5}. And the difference in ionization probability by using 15 and 20 angular momenta is 8.2×10^{-5}. Thus, 15 angular momenta and 1024 momentum grids were adopted in the calculations.

3. Results and discussions

We calculated the effects of laser pulses on the lithium atom by using the Gaussian-shaped pulse. The electric field and vector potential are

$$\vec{E}(t) = \hat{z}\, E_{\max} \mathrm{e}^{-2(\ln 2)(t/\sigma)^2} \sin(\omega t), t \in (-T/2, T/2),$$
$$\vec{A}(t) = -\int_{-\frac{T}{2}}^{t} \vec{E}(t')\, \mathrm{d}t'. \quad (7)$$

The FWHM is denoted as σ and ω is the laser central frequency. To simulate the vanishing of the pulse tails at $t = \mp\infty$, we adopted the ratio $E(t = \mp T/2)/E_{\max}$ to be 10^{-6}. Thus, the pulse duration is $T = \sigma\sqrt{6}\sqrt{2\ln 10/\ln 2} \sim 6.314\,\sigma$. Figure 1 shows an example of the profiles of field and vector potentials at peak intensity $I_0 = 12$ TW cm^{-2}. The FWHM is 10 fs and the wavelength is 785 nm. The calculated results show that the difference between using Gaussian and cosine-squared enveloped pulses at the same FWHM and same intensity is negligible. Thus, in the volume averaged results, we used the cosine-squared pulse to save computing time. The electric field of the cosine-squared pulse is as follows:

$$\vec{E}(t) = \hat{z}\, E_{\max} \cos^2(\pi t/T) \sin(\omega t), \quad t \in (-T/2, T/2). \quad (8)$$

For FWHM $= \sigma$, the pulse duration is $T = 2.7468\,\sigma$. The associated vector potential $A(t)$ can be found analytically.

3.1. Simulations of the experimental results

To simulate the experimental PADs, we applied a 30 fs FWHM cosine-squared pulse at a wavelength of 785 nm to the lithium atom. The focal volume averaging procedure was described in [17]. Figure 2 shows a plot corresponding to the experimental results shown in figures 3, 5 and 7 of [2]. The calculated data agree with the experimental results. As the volume averaging is weighted by the sliced isointensity volume elements of a pulse, the analysis of each peak power case becomes

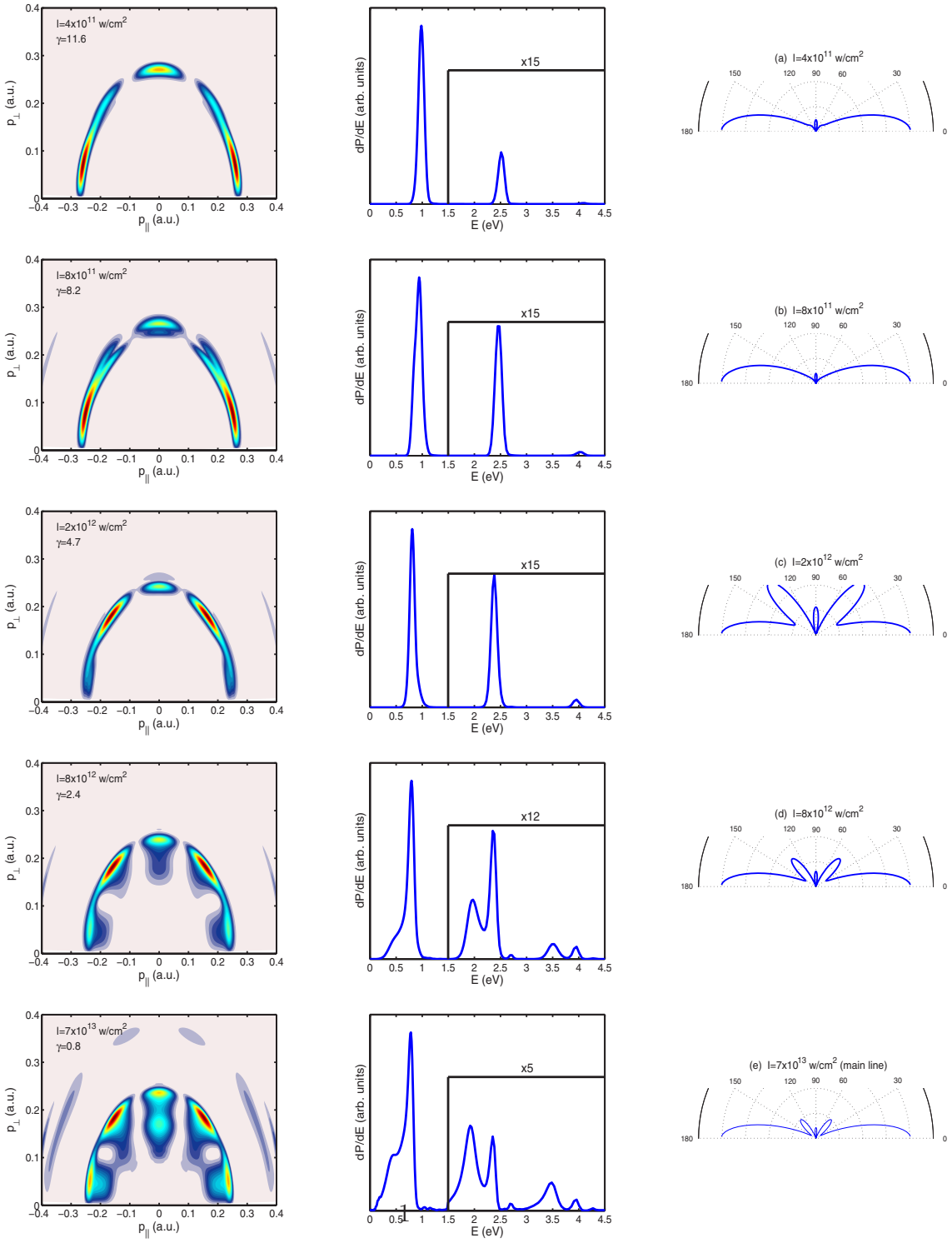

Figure 2. Focal-volume averaged two-dimensional electron momentum distributions are in the first column, corresponding ATI spectra and photoelectron angular distributions are in the second and third columns. The laser intensity labelled in the plot is to compare the experimental data. Graphs in the same row are results of the same intensity.

involved with intensity components. To elucidate the effect of the individual pulse with a specific peak power, we analyse the data below without using the focal volume average. For peak intensities smaller than $\sim$3 TW cm^{-2}, the photoelectron spectra show only the NRMPI of four-photon or more photon absorption from the 2s ground state. For intensities higher than $\sim$3 TW cm^{-2}, a peak around electron energy $E_e \sim 0.7$ eV and another lower than 0.7 eV always exist. The peak around 0.7 eV appeared at higher intensities, as the experimental results show. This ATI peak can be attributed to the three-photon absorption

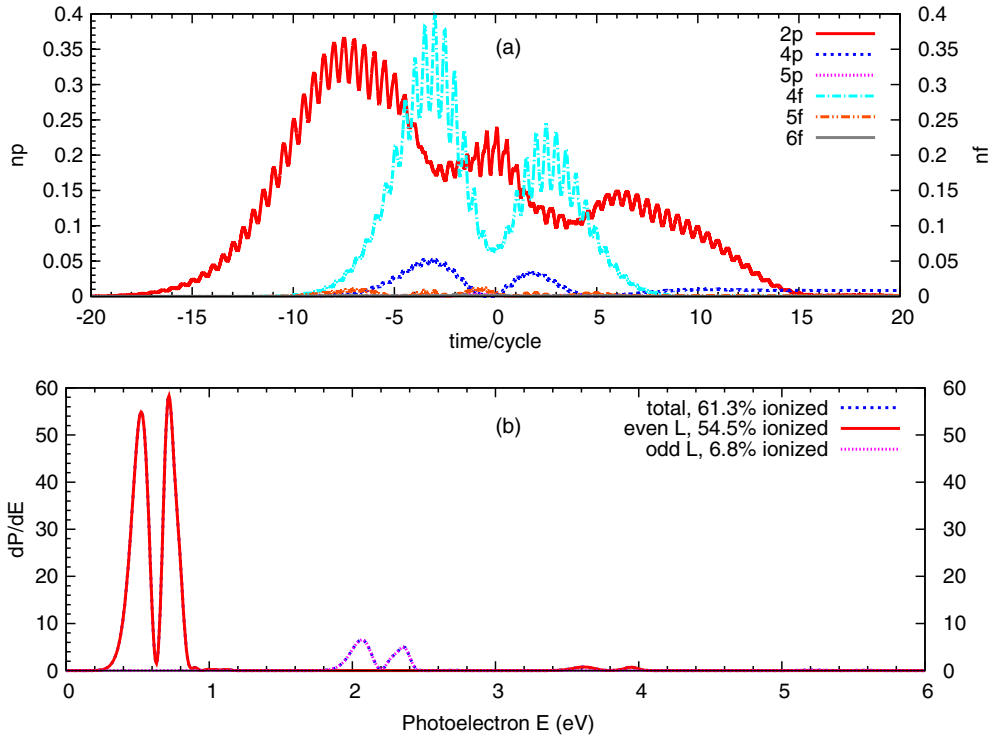

Figure 3. (a) Population history of some low-lying *n*p, *n*f-states under a 30 fs FWHM, 785 nm wavelength Gaussian pulse at peak intensity of 4 TW cm^{-2}. (b) The corresponding above-threshold ionization spectrum.

from 2s into 4p and 4f states, and subsequently, one additional photon is absorbed into the continuum. These are the REMPI processes. The ac Stark shift for an excited state and the threshold is known as the ponderomotive energy; the ATI peak energy remained the same as the intensity increased. The associate lower energy ATI peak is relevant. The mechanism is explained further in the following subsection.

3.2. Three-level coupling for intensities around and above 3 TWTW cm^{-2}

The energy levels of 4p, 4f are −0.87 and −0.85 eV, respectively. Figure 3(a) shows the population history of some low-lying *n*p and *n*f state below 4 TW cm^{-2}, 30 fs FWHM, 785 nm wavelength Gaussian pulse. The significant probabilities of the 4p, 4f state appear at approximately the time of $\mp(2 \sim 3)$ optical cycle and are depleted after the time of +5 cycle. The levels of 4p and 4f are nearly degenerate and are coupled with one photon into a ϵd state in the continuum. The three states form a $\Lambda-$ system [18]. By neglecting the small 0.02 eV difference between 4p and 4f, the interference of the $\Lambda-$ system causes the degenerate level to shift 0, and $\frac{W_p^2+W_f^2}{-\Delta}$, where

$$W_p = \frac{f(t)}{2}\langle\Psi_{4p}(\vec{p})|p_z|\Psi_{\epsilon d}(\vec{p})\rangle,$$
$$W_f = \frac{f(t)}{2}\langle\Psi_{4f}(\vec{p})|p_z|\Psi_{\epsilon d}(\vec{p})\rangle,$$
$$A(t) \simeq f(t)\cos(\omega t), \qquad (9)$$

and Δ is the detuning between the photon energy ω and the energy spacing $E_{\epsilon d} - E_{4p,4f}$. Figure 3(b) shows the ATI spectrum. The peak at 0.524 eV comes from the absorption of a photon from the downshifted level and the peak at 0.72 eV is from one-photon absorption at the unshifted level. Further absorption peaks in continuum were observed.

3.3. Multiphoton ionization spectra of 12 TW cm^{-2} at 30 and 10 fs FWHM

Figures 4(a) and (b) depict the population history of low-lying $l = 0 \sim 3$ states under the pulse with a peak power 12 TW cm^{-2} and 30 fs FWHM . The 2s ground state depleted to nearly 10% at approximate the time of −7 cycle. The ionization mechanism is a four-photon absorption process in an even angular momentum continuous state. At the approximate time of −7 cycle, the ponderomotive energy is ∼0.6 eV instead of 0.69 eV at peak power. The populations for excited states are noticeable. They are populated before the field rises to peak value and mostly disappear after the peak value. This means that portions of ionization derive from these excited states. The REMPI through excitations to $n = 4$ is the main mechanism from the excited state history. The calculated ionization probability is 96.2%. Figure 4(c) shows the bound state probability multiplied by the cubic power of its principal quantum number n. The absorption of one photon from 4p, 4f state (energy level −0.85 eV), and a minor contribution from 5p (−0.5545 eV) and 5f (−0.5442 eV) contribute to the ATI. The $n^3 \times probability$ of the bound state near energy = 0 is connected to the continuous part [19]. Figure 4(d) shows the ATI spectrum with a separate plot of even and odd angular momenta. The first peak designated by A at 0.35 eV comes from the four-photon absorption at approximately the time of

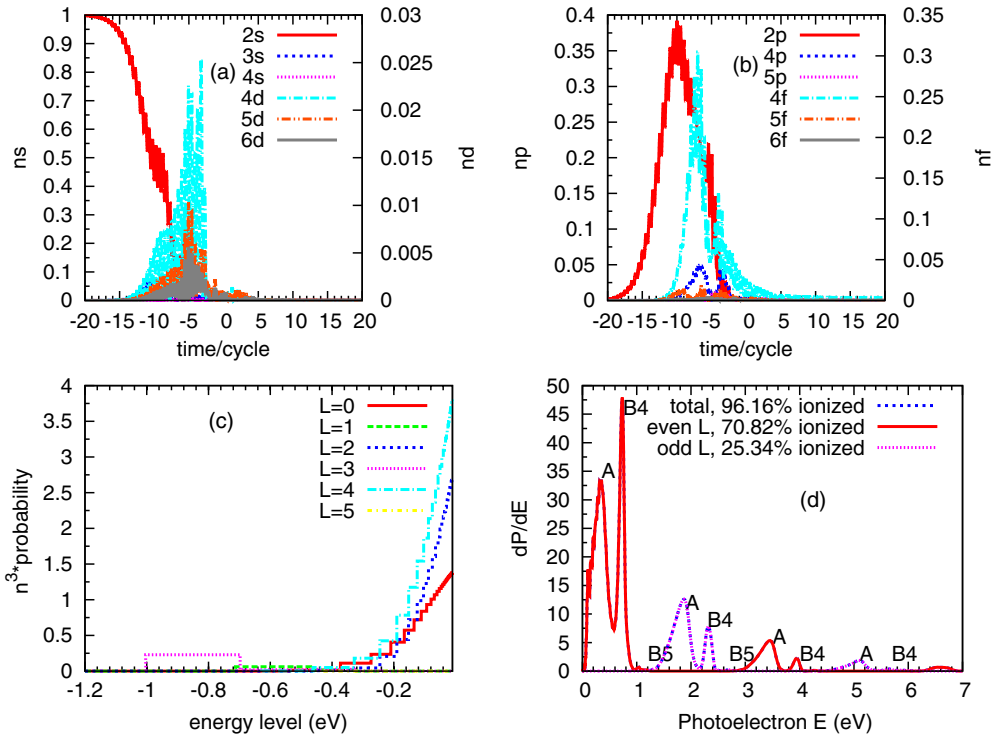

Figure 4. (a) Population history of some low-lying *n*s, *n*d states. (b) Population history of some low-lying *n*p, *n*f states. (c) $n^3\times$(probability of bound state) for $l = 0 \sim 5$. (d) The corresponding ATI spectrum of 12 TW cm^{-2} 30 fs FWHM, 785 nm wavelength Gaussian pulse.

-6 cycle of the 2s ground state. The absorption of additional photons generates the ATI corresponding group A peaks with odd and even angular momenta alternatively. The lowest B4 peak comes from the absorption of one photon mainly at the 4p, 4f levels. The B5 smaller peak at approximately 1.1 eV comes from the absorption of one photon at the 5p and 5f levels as shown in figure 4(b). Subsequent B groups absorb more photons.

In the 30 fs FWHM case, the frequency width of the laser pulse is approximately 0.06 eV. The ATI spectrum is simpler than for a short duration pulse, because less resonant excitation to intermediate bound states can occur than when the pulse has a wider bandwidth. Regarding the case of a 10 fs FWHM pulse at the same intensity next to where the bandwidth is approximately 0.2 eV: figures 5(a) and (b) show the state population history. The ground state 2s is depleted to $\sim$20% at approximately 2.3 cycles before peak intensity and oscillates to vanishing near peak intensity. The four-photon absorption of the 2s state at different moments (hence different ponderomotive shifts) after -5 cycle becomes the ATI peaks designated as group A at the approximate energy of 0.35 eV [4]. Compared to the 30 fs case, the four-photon absorption of 2s closer to the peak power feels a larger ponderomotive shift than around the time of -5 cycle and results in an ATI peak with energy of 0.26 eV. The structures at approximately 0.7 eV (B4) and 1.04 eV (B5) are from the one-photon absorption of the 4p, 4f and 5f levels, respectively. Figure 5(c) shows the $n^3 \times probability$ of the bound state near energy $= 0$. More populations stay at highly excited states than in the 30 fs case. Figure 5(d) is the corresponding ATI spectrum. The absorption of additional photons from the lower energy groups A, B4 and B5 produce higher corresponding groups with odd and even angular momenta alternatively.

For a peak intensity of 12 TW cm^{-2}, the Keldysh parameter is $\gamma \sim 2$. Based on the above-mentioned study, the ground state is depleted before the peak intensity. The depletion occurs even earlier for a stronger intensity of $\gamma = 1$, which was used as a criterion for TI. Clearly, the conventional use of γ to classify the ionization mechanism is not useful in the case of the lithium atom.

In a laser field, the atomic ground state energy shifts slightly, but the excited and ionization threshold shift upward through the ponderomotive energy [20]. Figure 6 shows a plot of the ATI spectra of Li under 30 fs FWHM with peak powers of 2 and 12 TW cm^{-2}. At 2 TW cm^{-2}, the field is not sufficiently strong for the 2s ground state to absorb four photons. Based on the population history (not shown), the first ATI peak (0.74 eV) comes from the REMPI absorption of one photon from 4p, 4f state and the absorption of one additional photon is the odd angular momentum ATI peak at 2.31 eV. For the 12 TW cm^{-2} case, the first ATI peak at 0.35 eV comes from the four-photon absorption from the 2s ground state with the effect of the threshold being upshifted by ponderomotive energy before reaching peak intensity. The ATI peak at 0.734 eV is attributed to the REMPI absorption of one photon from the 4p, 4f state. Although the ponderomotive energies are different in the 2 and 12 TW cm^{-2} cases, the ATI peaks from the excited state (4p, 4f in this case) are identical. This confirms the theory of atomic level shift under the laser pulse and is elucidated by the photoionization spectra.

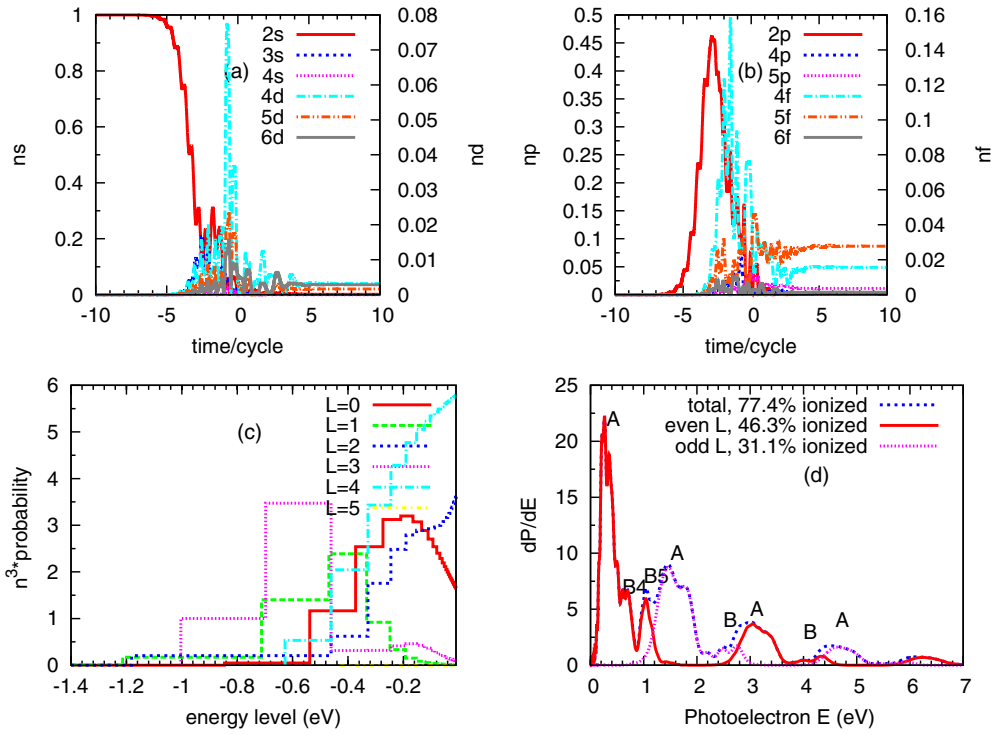

Figure 5. (a) Population history of some low-lying *n*s, *n*d states. (b) Population history of some low-lying *n*p, *n*f states. (c) $n^3 \times$(probability of bound state) for $l = 0 \sim 5$. (d) ATI spectrum of 12 TW cm^{-2} 10 fs FWHM, 785 nm wavelength Gaussian pulse.

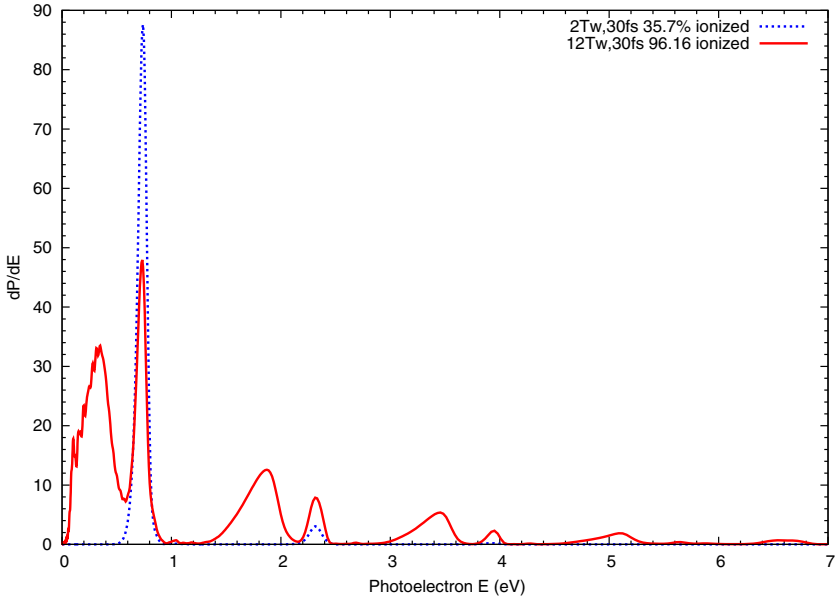

Figure 6. ATI spectra of 2 and 12 TW cm^{-2} Gaussian pulses at FWHM 30 fs, 785 nm wavelength.

3.4. Change of ionization with intensity

Figure 7(a) shows the Keldysh parameter γ versus the ratio of states with principal quantum number $n \geqslant 5$ to all bound states, for pulse durations of 6, 10 and 30 fs. In the 30 fs case, the ratio rises to 0.9, with the intensity increasing up to $\gamma \sim 2$, (13 TW cm^{-2}) and increasing to nearly 1 with even stronger field. The ratio is then suppressed slightly at $\gamma \sim 0.5$. Figure 7(b) shows the changes of γ at the corresponding probability for ionization, bound states with $n \leqslant 4$, and with $n \geqslant 5$ respectively. The plots show that the ionization probability is saturated and then suppressed at intensities greater than 13 TW cm^{-2}. Because of the persistent occupation of $n \geqslant 5$ Rydberg state with strong intensity, the ionization probability does not increase with intensity. The unusual stability of the Rydberg states is not strange but is simply

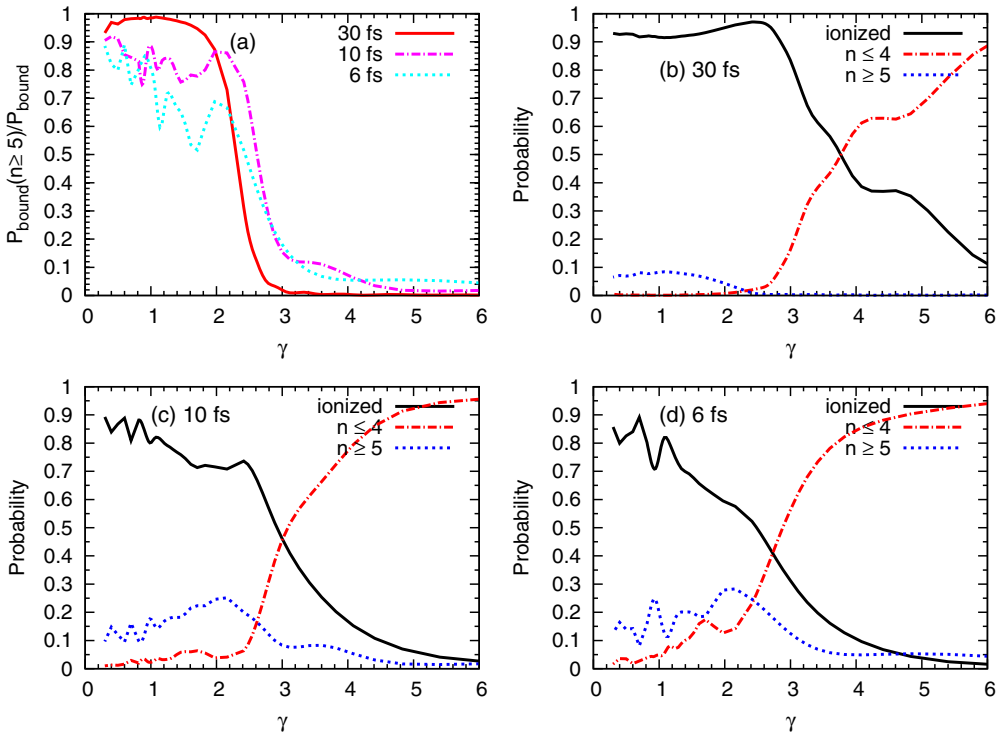

Figure 7. (a) Probability ratio of bound state $n \geqslant 5$ to all bound state versus Keldysh parameter γ. (b) Probability of ionization, bound state with $n \geqslant 5$, bound state with $n \leqslant 4$ for FWHM 30 fs. (c) Same as (b) for FWHM 10 fs. (d) Same as (b) for FWHM 6 fs. The wavelength is 785 nm for all cases.

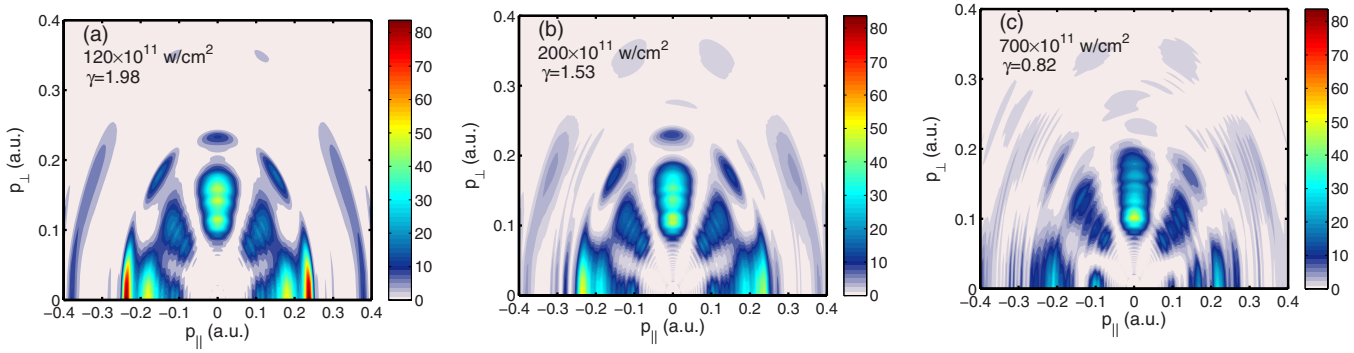

Figure 8. (a) Photoelectron angular distribution $|\Psi(p_\parallel, p_\perp)|^2$ for 12 TW cm^{-2}. (b) Same as (a) for 20 TW cm^{-2}. (c) Same as (a) for 70 TW cm^{-2}. All cases use 30 fs FWHM 785 nm wavelength.

the high-frequency stabilization effect [21, 22]. Because the timescale of the Rydberg states is in the microwave range, whereas the 785 nm IR laser is at a much higher frequency than those of microwaves, the excitation effect on these Rydberg states is negligible.

Noticeable fluctuations of the population ratio of $n \geqslant 5$ to all bound states with intensity of 10 and 6 fs pulses were found, as shown in figure 7(a). To interpret this effect we plotted the probability of ionization and the bound states with $n \leqslant 4$ and with $n \geqslant 5$ as shown in figures 7(c) and (d). For the shorter duration pulses of 6 and 10 fs, the corresponding band widths are larger than a long pulse. The probability of resonant excitations to excited states during the multiphoton absorption enhanced. Furthermore, the ponderomotive energy is proportional to the laser intensity. When the multiphoton energy plus the ponderomotive shift hits intermediate bound levels, resonant excitations occur. As intensity changes, the resonance might be lost and further increasing the intensity might achieve other resonances. This effect occurs more easily for a short pulse than for a long pulse [23].

3.5. The fan-like structure in photoelectron angular distributions for strong fields

For intensities larger than 8 TW cm^{-2} as shown in figure 5 of [2], fan-like structures form in the PADs because of the long-range Coulomb interaction between ionized electron and its parent ion. The stronger field has a larger ponderomotive

energy than a low laser intensity case does and the larger ponderomotive energy induces more REMPI and thus, more rings in PAD to form the fan-like structure. Figure 8 shows that, in PADs of 30 fs FWHM pulses at intensities of 12 ($\gamma = 1.98$), 20 ($\gamma = 1.53$) and 70 ($\gamma = 0.82$) TW cm^{-2}, the fan-like structure in $p_\perp$ remained unchanged, whereas the probability in $p_\parallel$ decreased as the intensity increased. This is because the electron wavepacket is driven mainly in the direction of polarization and therefore might collide with the parent ion and be scattered into Rydberg states which are stabilized under high-frequency laser field. Figure 7(b) shows that, as the intensity increased to the $\gamma < 2$ regime, the population of Rydberg states of $n \geqslant 5$ increased and stabilized, thus causing the suppression of ionization in such regime.

4. Conclusion

In this study, we investigated the strong-field ionization of the lithium atom by calculations in momentum space. The ATI spectral peaks were identified based on state population history and energy levels. We demonstrated the roles that pulse duration and ponderomotive shift play in the resonance enhanced multiphoton ionization processes. For a FWHM 30 fs pulse at strong intensity, the ionization probability is saturated and then suppressed by increasing the intensity. For FWHM 10 and 6 fs pulses, the ionization probability fluctuates by increasing the intensity. Both of these results were caused by the resonance excitation into intermediate Rydberg states and remained high-frequency stabilized as shown in figure 7. Regarding the fan-like structure in the high intensity regime, the photoelectron probability decreased in the polarization direction, but remained unchanged in the perpendicular direction. This effect is also caused by the electron rescattering into the Rydberg states in the field driving direction. Finally, as the results indicate, the ground state is depleted before peak intensity is achieved. In other words, the ground state electron never experienced the peak intensity; hence, the Keldysh parameter, defined according to the peak intensity, is not meaningful in this case.

Acknowledgments

The authors thank Professor Chii-Dong Lin for helpful comments. The work is supported by the National Science Council of Taiwan under contract number NSC100-2112-M-009-006-MY3.

References

[1] Jiang T-F, Jheng S-D, Lee Y-M and Su Z-Y 2012 *Phys. Rev.* E **86** 066702
[2] Schuricke M, Zhu G, Steinmann J, Simeonidis K, Ivanov I, Kheifets A, Grum-Grzhimailo A N, Bartschat K, Dorn A and Ullrich J 2011 *Phys. Rev.* A **83** 023413
[3] Freeman R R, Bucksbaum P H, Milchberg H, Darack S, Schumacher D and Geusic M E 1987 *Phys. Rev. Lett.* **59** 1092
[4] Wickenhauser M, Tong X M and Lin C D 2006 *Phys. Rev.* A **73** 011401
[5] Arbo D G, Yoshida S, Persson E, Dimitriou K I and Burgdorfer J 2006 *Phys. Rev. Lett.* **96** 143003
[6] Chen Z, Morishita T, Le A T, Wickenhauser M, Tong X M and Lin C D 2006 *Phys. Rev.* A **74** 053405
[7] Jiang T-F and Chu S-I 1992 *Phys. Rev.* A **46** 7322
[8] Telnov D A and Chu S-I 2009 *Phys. Rev.* A **79** 043421
[9] Telnov D A and Chu S-I 2011 *Phys. Rev.* A **83** 063406
[10] Tao L and Scrinzi A 2012 *New J. Phys.* **14** 013021 and references therein
[11] Kwon Y R and Tabakin F 1978 *Phys. Rev.* C **18** 932 (reference 8)
[12] Zhou Z and Chu S-I 2011 *Phys. Rev.* A **83** 013405
[13] Tong X M and Chu S-I 1997 *Chem. Phys.* **217** 119
[14] Schweizer W, Faßbinder P and González-Férez R 1999 *At. Data Nucl. Data Tables* **72** 33
[15] http://physics.nist.gov/PhysRefData/ASD/levels/_form.html
[16] Wiese M L and Fuhr J R 2009 *J. Phys. Chem. Ref. Data* **38** 565
[17] Morishita T, Chen Z, Watanabe S and Lin C D 2007 *Phys. Rev.* A **75** 023407
[18] Band Yehuda B 2006 *Light and Matter* (West Sussex: Wiley) section 9.3
[19] Friedrich H 2006 *Theoretical Atomic Physics* (Berlin: Springer) section 3.2.3
[20] Chu S-I and Cooper J 1985 *Phys. Rev.* A **32** 2769
[21] Pont M and Gavrila 1990 *Phys. Rev. Lett.* **65** 2362
[22] Jiang T F 1993 *Phys. Rev.* A **48** 3995
[23] Jones R R 1995 *Phys. Rev. Lett.* **74** 1091